Volume 1, Issue 2, pp 24 - 46, year 2024

Journal of the Egyptian Society for Basic Sciences-Physics (JESBSP)

https://jesbsp.journals.ekb.eg/

The influence of Manganese doping on structural , thermal and conduction properties of nano Nickel Zinc ferrites

M. Abdel Hakim[1], O.M. Hemeda[1*], F. Elhoseny[1], G. Zidan[1], A. M. A Henaish[1, 2], Y.A. Alibwaini[3] **and M. Mostafa[1]**

1 Tanta University, Faculty of science , Physics Department
2 NANOTECH Center, Ural Federal University, Ekaterinburg 620002, Russia
3 Department of communication and computer engineering , Gadara university ,Irbid 21110,Jordan
*Corresponding author: O.M. Hemeda email: omhemeda@yahoo.co.uk

Abstract

The current work involves the use of flash auto combustion procedure to synthesize nano-ferrites $Ni_{0.3}Zn_{0.7-x}Mn_xFe_2O_4$, (x = 0.00, 0.15, 0.25, 0.35, 0.45, and 0.55) annealed at 800°C for 4h. X-ray diffraction, XRD, pattern analysis verified the structure phase. The Rietveld observed peaks correspond to two phases; spinel ferrites, belong to the Fd-3m space group, and hematite belongs to the R-3c space group. The thermogram (TGA) of the as prepared samples in the temperature range from 50 to 1000°C and showed two distinct regions. The small weight loss value was noticed in our sample in both regions is due to the structural stability for the as prepared sample which confirm by x-ray data analysis. The grain size decreased by increasing Mn content from 0.74 to 0.33 μm. The M" curve increases with applied frequency showing relaxation peak and ends with sharp decrease at high frequency. The cole-cole diagram illustrates the presence of semi-circles depending on the presence of the relaxation effect at low frequency. The diameter of semi-circles decreases by the increasing of the Mn content from 5.3 to 1.25 cm. At low frequency region the conductivity is constant and almost equal zero representing σ´ is frequency independent (DC conductivity) up to10^3 Hz then it starts to increase gradually with the increase of frequency showing some dispersion. Also, the conductivity increases with the increase of Mn content. The value of Z′ at different Mn^{2+} concentrations overlap at particularly high frequencies which refers to the probable liberation of space charges.

Keywords: Ferrites, auto combustion, XRD, SEM, TGA and cole-cole diagram.

Declarations: The authors have no relevant financial or non-financial interests to disclose.

1. Introduction:

Ferrite nanoparticles have garnered significant attention for their prospective utility in various fields, including photocatalysis, water-gas shift reactions, and sensor technology. Because of the disparity in size and charge between the metal ions and the balanced charge of oxygen, ferrites are typically found in one of three distinct structures: garnet, hexagonal, and spinel. Among these, spinel structures with the formula MFe_2O_4 are particularly appealing. Here, M represents a divalent metal cation such as Mn, Co, Ni, Cu, Zn, Mg, or a combination of these ions. Soft ferrites, specifically spinel ferrites with cubic crystal geometry, have become a focal point of interest owing to their exceptional physico-chemical properties and wide-ranging applications across various domains. The spinel structure, belonging to space group Fd3m, features a face-centered cubic (f.c.c) unit cell with eight formula units per unit cell ($M_8Fe_{16}O_{32}$). Within each unit cell of ferrite, there are 96 interstices, comprising 64 tetrahedral and 32 octahedral sites, nestled between the closely packed oxygen atoms. However, only 8 tetrahedral and 16 octahedral positions are occupied by the cations, denoted as (A) and (B) sites, respectively. The distribution of each metal ion is determined by its affinity for both positions, influenced by factors such as stabilization energy, ion radius, interstice size, synthesis method, and synthesis conditions. The type and distribution of cations at these tetrahedral and octahedral sites significantly impact the physical and chemical properties of ferrite nanoparticles. Ferrites are favored materials across numerous applications because of their affordability, strong resistance to corrosion, and favorable magnetic properties. Transition metal ferrites, in particular, hold significant importance in both economic and engineering contexts owing to their effective physical attributes. At the nano-scale level, spinel ferrites exhibit distinct structural, chemical, physical, and magnetic characteristics, along with unique dielectric properties, setting them apart from their bulk counterparts. These attributes make them particularly promising for high-frequency applications. The physical properties of spinel ferrites are influenced by factors such as the distribution of metal ions in different lattice sites, reaction and sintering temperatures, and the method of preparation [1-5].

A variety of methods have been used to synthesize soft spinel ferrite materials, including chemical co-precipitation [6], hydrothermal method [7], mechano-chemical method [8], microemulsion method [6], rheological phase reaction method [9], sol-gel method [10], flash auto combustion method [11], and thermal decomposition of some precursors [12].The co-precipitation approach is frequently utilized because it produces nanoparticles with a consistent size distribution and provides for easy control over synthesis settings and nucleation development [13]. The solgel technique may produce multi-component spinel oxides with high purity and homogeneous composition [13]. Mn-Zn ferrites are commonly utilized in electronic applications due to their high permeability and low magnetic losses at high frequencies. Ferrites' characteristics are generally determined by their microstructure; hence the nano-technique is provided as an alternative to the traditional ceramic method for controlling their ultra-microstructure [14].

Ni-Zn and Mn-Zn nanoferrites play pivotal roles in various technological applications, particularly in magnetic cores utilized in high-speed digital recording read-write heads. Their

exceptional magnetic properties make them preferred choices for such demanding tasks. Moreover, there's a growing interest in understanding the magnetic properties and magnetoelectronic transport behavior of Ni-Mn ferrites. In particular, the magnetic properties of diamagnetically substituted ferrites, such as Ni-Zn and Mn-Zn variants, have garnered significant attention due to their relevance in high-frequency applications. In addition to their magnetic functionalities, Ni-Zn-Mn ferrites exhibit advantageous electrical and mechanical properties, making them suitable for diverse applications in modern technology. Their chemical stability, corrosion resistance, and cost-effectiveness further enhance their attractiveness for industrial and commercial use. Researchers are keen on exploring and enhancing these properties to meet the demands of emerging technologies and advance magnetic materials for various industrial and commercial applications[15-17].

2. Experimental details

2.1. Sample preparation:

In this work, A series of $Ni_{0.3}Zn_{0.7-x}$ $Mn_xFe_2O_4$ (x=0.00, 0.15, 0.25, 0.35, 0.45, and 0.55) were prepared by the flash auto combustion method using nickel nitrate hexahydrate **($Ni(NO_3)_2.6H_2O$)**, zinc nitrate (**$Zn(NO_3)_2.6H_2O$**), manganese nitrate (**$Mn(NO_3)_2.6H_2O$**), ferric nitrate (**$Fe(NO_3)3.9H_2O$**) and urea **$CO(NH_2)_2$** as a fuel. The metal nitrates were combined with the urea by via a glass rod. The mixture was heated on the hot plate at 80°C, with continuous stirring to get a uniform viscous material, to achieve the proper temperature for combustion which transforms the material into powder. The powder was collected, annealed at 800°C for 4 hours, and then pressed into a tablet shape with a thickness of 0.35 cm at 5000 kg /cm^2. The samples were then subjected to the requisite electrical, dielectric, and thermal tests.

2.2. Physical measurements

The samples were examined by x-ray diffraction using a Philips model (PW-1729) diffractometer (Cu-Kα radiation source with λ = 1.540598 Å) with 2Θ in the range from 4° to 80°. The Rietveld refinement of XRD patterns was investigated utilizing (COD:9007270) to match and fit, using the software FullPROF and Vesta. Thermogravimetric analysis (TGA and its derivative) of these nano-ferrites is performed using model (SDT Q600 V20.9 Build 20). SEM is used to study the morphology of materials (JOEL, Model: JSM-5200 LV). Image J software was used to capture more than 30 ferrite particles with an average length, and the average grain and particle size of the treated samples were computed. The frequency-dependent electrical and dielectric characteristics of Ni-Zn/Mn spinel ferrites tablets were measured using a high-precision LCR meter bridge (HP-6284A).

3. Results and discussion

3.1 Rietveld Refinement of X-ray patterns:

The XRD patterns of $Ni_{0.3}Zn_{0.7-x}$ $Mn_xFe_2O_4$ (x=0.00, 0.15, 0.25, 0.35, 0.45, and 0.55) were carried out using the XRD technique and presented in **Fig. 1**. The Rietveld observed peaks

correspond to two phases; spinel ferrites, belong to the Fd-3m space group, and hematite belongs to the R-3c space group. With increased manganese concentration, the spinel ferrites phase weight slowly decreases from 93.4% to 81.9% while the hematite phase weight is relatively low and increases varying from 6.6% to 18.1%. The appearance of hematite is due to the heating of spinel ferrite in the air during the combustion reaction [18]. Therefore, the density of the spinel ferrite phase decreases with increasing the hematite phase which direct affect the lattice parameter. The lattice parameter and the volume of the two phases decreased due to the introducing of Mn^{2+} ions which possess a large ionic radius (0.82 Å) compared with zinc ions having a small ionic radius (0.72 Å) [1]. The values of lattice parameters, volume, density, and weight percentage of phases are given in **Table (1)**. Fe and Ni ions occupied both 8b and 16c sites. The occupations of iron ions are 0.430 and 1.57, and the occupation of nickel ions are 0.18 and 0.12, for both sites respectively for all samples. With increasing Mn ions concentrations, the occupation of Mn ions increases from 0.00 to 0.32 for the 8b site and from 0.00 to 0.23 for the 16c site, this leads to a decrease in the occupation of Zn ions in both 8b and 16c sites from 0.39 to 0.07 for 8b site and from 0.31 to 0.08 for 16c site. The Atomic parameter of O ions slowly increases with increasing manganese concentration. The structure parameters of $Ni_{0.3}Zn_{0.7-x}\ Mn_xFe_2O_4$ ferrites are tabulated in **Table (2)**.

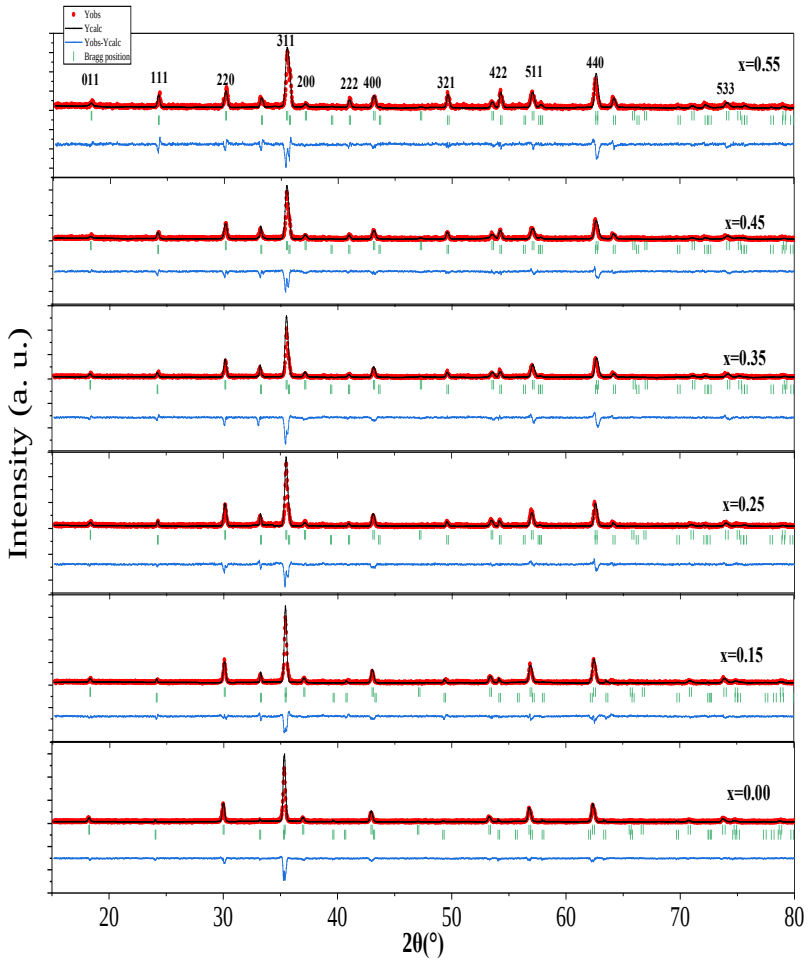

Fig. 1 The Rietveld refined XRD patterns of $Ni_{0.3}Zn_{0.7-x}\ Mn_xFe_2O_4$ ferrites.

Table (1) The values of lattice parameters, volume, density, and weight of phases for $Ni_{0.3}Zn_{0.7-x}Mn_xFe_2O_4$ ferrites.

x	Space group	Lattice parameter			Volume Å^3	Density (g/cm^3)	Weight%
		a Å	b Å	c Å			
0	Fd-3m	8.42093	8.42093	8.42093	597.146	5.319	93.37
	R-3c	5.08484	5.08484	13.65055	305.658	5.205	6.63
0.15	Fd-3m	8.40628	8.40628	8.40628	594.034	5.311	87.88
	R-3c	5.06966	5.06966	13.64914	303.804	5.237	12.12
0.25	Fd-3m	8.39559	8.39559	8.39559	591.771	5.299	84.38
	R-3c	5.02867	5.02867	13.73079	300.700	5.291	15.62
0.35	Fd-3m	8.37881	8.37881	8.37881	588.230	5.317	82.16
	R-3c	5.02375	5.02375	13.70979	299.652	5.310	17.84
0.45	Fd-3m	8.38397	8.38397	8.38397	589.318	5.283	83.81
	R-3c	5.02616	5.02616	13.71440	300.040	5.303	16.19
0.55	Fd-3m	8.38475	8.38475	8.38475	589.482	5.258	81.86
	R-3c	5.02298	5.02298	13.70444	299.444	5.314	18.14

Table (2) The structure parameter of $Ni_{0.3}Zn_{0.7-x}Mn_xFe_2O_4$ ferrites.

X	atom	site	Atomic parameter (X=Y=Z)	Occupation
0.00	Fe	8b	0.375	0.43
		16c	0	1.57
	Ni	8b	0.375	0.18
		16c	0	0.12
	Zn	8b	0.375	0.39
		16c	0	0.31
	Mn	8b	0.375	0
		16c	0	0
	O	32e	0.24788	1
0.15	Fe	8b	0.375	0.43
		16c	0	1.57
	Ni	8b	0.375	0.18
		16c	0	0.12
	Zn	8b	0.375	0.31
		16c	0	0.24
	Mn	8b	0.375	0.08
		16c	0	0.07
	O	32e	0.24945	1

0.25	Fe	8b	0.375	0.43
		16c	0	1.57
	Ni	8b	0.375	0.18
		16c	0	0.12
	Zn	8b	0.375	0.26
		16c	0	0.19
	Mn	8b	0.375	0.14
		16c	0	0.11
	O	32e	0.25086	1
0.35	Fe	8b	0.375	0.43
		16c	0	1.57
	Ni	8b	0.375	0.18
		16c	0	0.12
	Zn	8b	0.375	0.20
		16c	0	0.15
	Mn	8b	0.375	0.19
		16c	0	0.16
	O	32e	0.25323	1
0.45	Fe	8b	0.375	0.43
		16c	0	1.57
	Ni	8b	0.375	0.18
		16c	0	0.12
	Zn	8b	0.375	0.13
		16c	0	0.12
	Mn	8b	0.375	0.26
		16c	0	0.19
	O	32e	0.25636	1
0.55	Fe	8b	0.375	0.43
		16c	0	1.57
	Ni	8b	0.375	0.18
		16c	0	0.12
	Zn	8b	0.375	0.07
		16c	0	0.08
	Mn	8b	0.375	0.32
		16c	0	0.23
	O	32e	0.25161	1

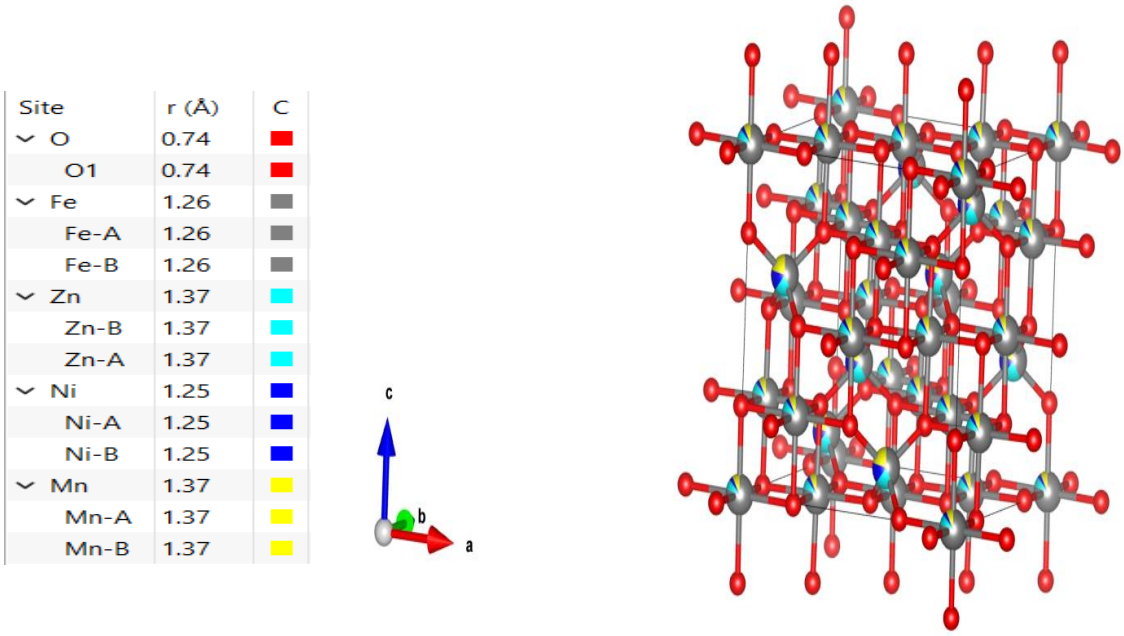

Fig (2) Rietveld refinement diffraction planes of Ni0.3Zn0.7-xMnxFe2-xO4 samples

Rietveld refinement diffraction peaks corresponding to diffraction planes (220), (311), (222), (400), (331), (422), (333), (511), (400), (531), (422), (620), (533), and (622) are indexed according to fcc spinel structure shown in Fig. 2 was drawn using VESTA software. The values lattice parameter a(Å), cell volume and density, for all samples , calculated by Rietveld refinement were given in **table 1**.

Table .3 . The crystallite size and partixle size of **of Ni0.3Zn0.7-xMnxFe2-xO4 samples**

x	D (nm)	**Particle size (nm)**
0		51.8±17.3
0.15	34.12	21.7±5.5
0.25	32.55	24.4±7.0
0.35	31.80	21.1±7.2
0.45	31.51	27.2±13.6
0.55	29.27	23.5±5.2

The values of crystallite size and particle size are taken from our previous work under publication . The scattered values of particle size can be explained by the two opposite effects of Mn , its retard and agglomeration effects.

3.2 Thermal Gravimetric Analysis (TGA):

Fig. 3 shows the thermogram (TGA) of the as prepared $Ni_{0.3}Zn_{0.7-x}Mn_xFe_2O_4$ (x=0,0.15,0.25,0.55) in the temperature range from 50 to 1000°C and shows two distinct regions [19] in **Table (3)**. The first stage from 50-200°C in which the water evaporation occurs while the second stage from 200 to 850°C is due to the evaporation of volatile product and the degradation of organic phase present in the sample during preparation. The first stage weight loss has the value range from 1 to 3 mg whereas for the second stage the weight loss ranges from 0.4 to 7 mg. The end of the second stage for the studied sample shift to higher temperature which confirm the increase of the thermal stability by increase Mn content. The small weight loss value was noticed in our sample in both region is due to the structural stability for the as prepared sample which confirm by x-ray data analysis. The weight loss for the second region increases by increasing Mn content from 0.4 to 7% indicating that the non-decomposed residue (nitrates, organic matters) increases by increasing Mn content in the given ferrite.

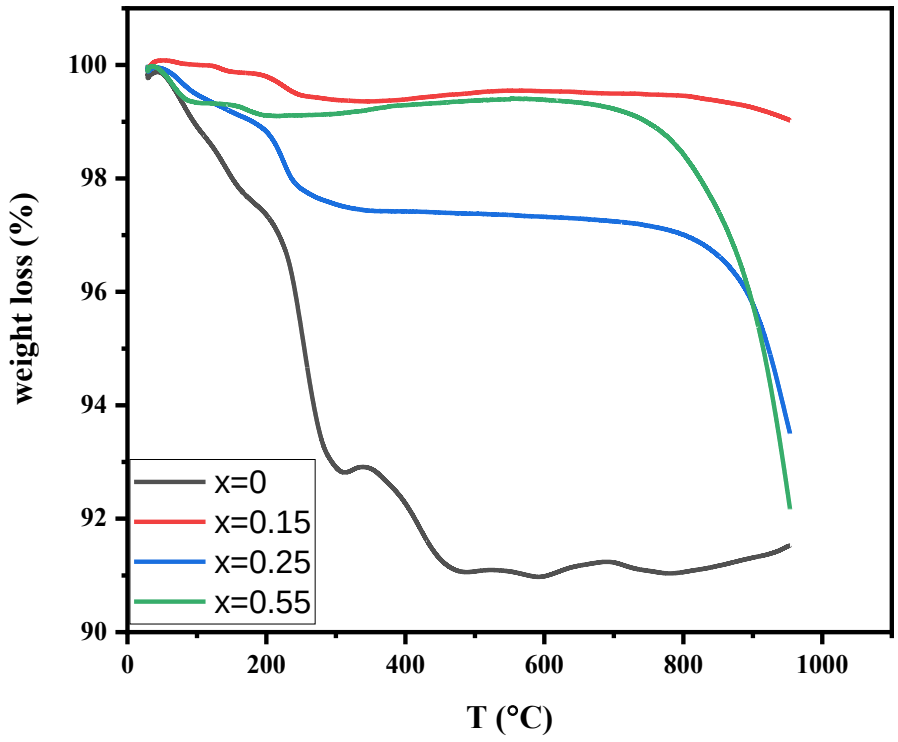

Fig. 3 TGA curves of $Ni_{0.3}Zn_{0.7-x}Mn_xFe_2O_4$ samples (x=0,0.15,0.25,0.55).

Table (4) weight loss of two regions of $Ni_{0.3}Zn_{0.7-x}Mn_xFe_2O_4$ samples (x=0, 0.15, 0.25, 0.55).

x	First Region		Second Region	
	ΔT (°C)	Weight Loss (%)	ΔT(°C)	Weight Loss (%)
0	50-200	3	Not observed	-
0.15	50-200	2.5	200-800	0.4
0.25	50-200	2.5	250-830	3.5
0.55	50-200	1	200-850	7

3.3 SEM analysis:

Fig. 4 shows the SEM micrographs for the sample $Ni_{0.3}Zn_{0.7-x}Mn_xFe_2O_4$ (x=0,0.15,0.25,0.35,0.45 0.55) synthesized by auto combustion flash annealed at 800°C for 4h. It was found that the grain nature of the sample confirms the polycrystalline properties of the sample surface. The average grain size was measured by image j software [20] and is given in **Table (4)**. The results show the decrease of grain size by increasing Mn content due to the presence of Mn ion which acts as grain gross inhibitor. The manganese ions exhibit insolubility within the lattice, causing them to amass at the grain boundaries. This accumulation results in a reduction in grain size and hinders the growth of the grains. As the Mn content increases, the grain size decreases, resulting in larger grain size boundaries. SEM analysis indicates a reduction in porosity with increasing Mn content, contributing to the reduction in grain diameter [21]. The micrographs reveal that the grain size is separated by pores which is clearly decrease by increasing Mn content, these phenomena is confirmed by x-ray analysis which state that the porosity decreased by increasing Mn content.

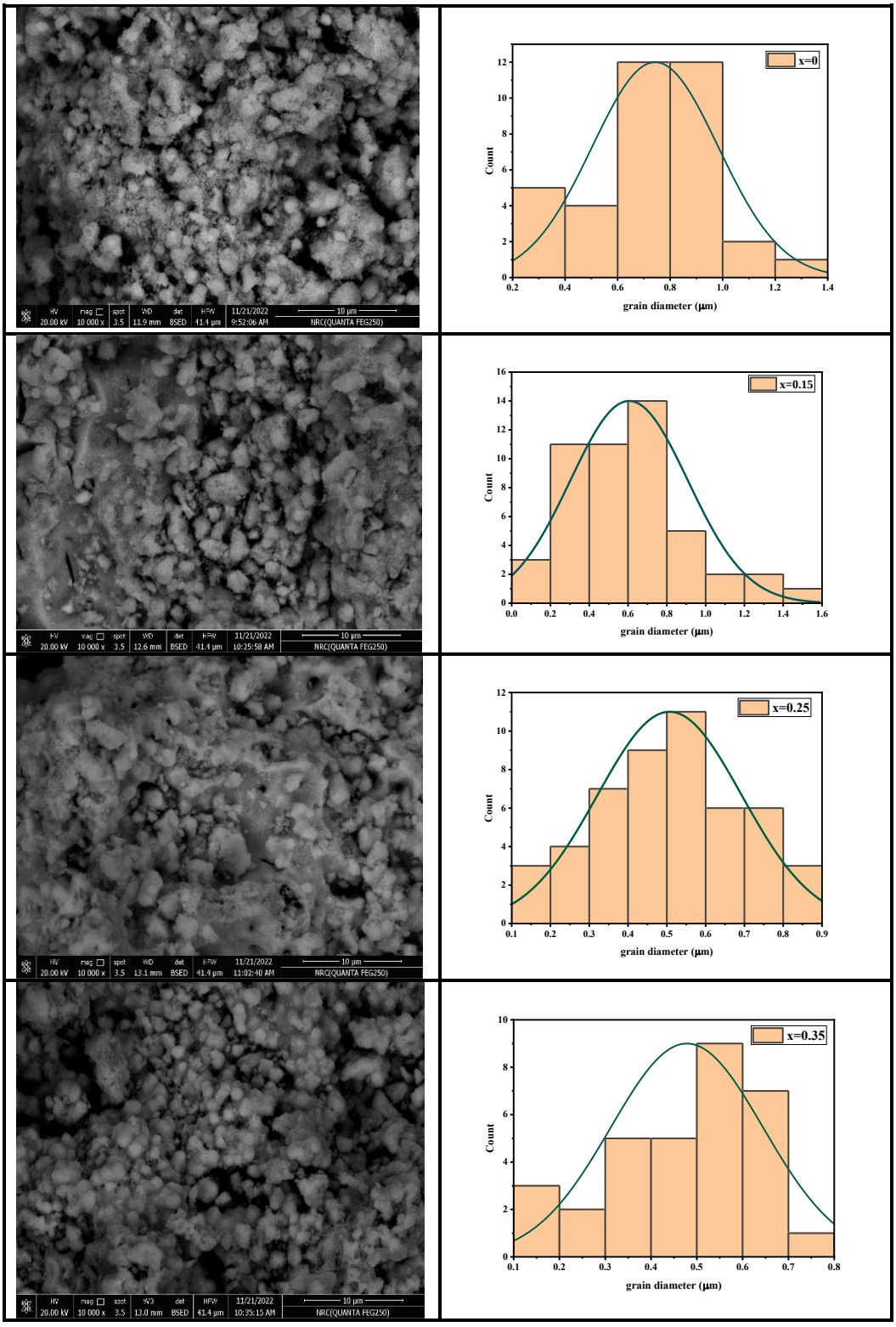
x=0
Count
grain diameter (µm)
x=0.15
Count
grain diameter (µm)
x=0.25
Count
grain diameter (µm)
x=0.35
Count
grain diameter (µm)

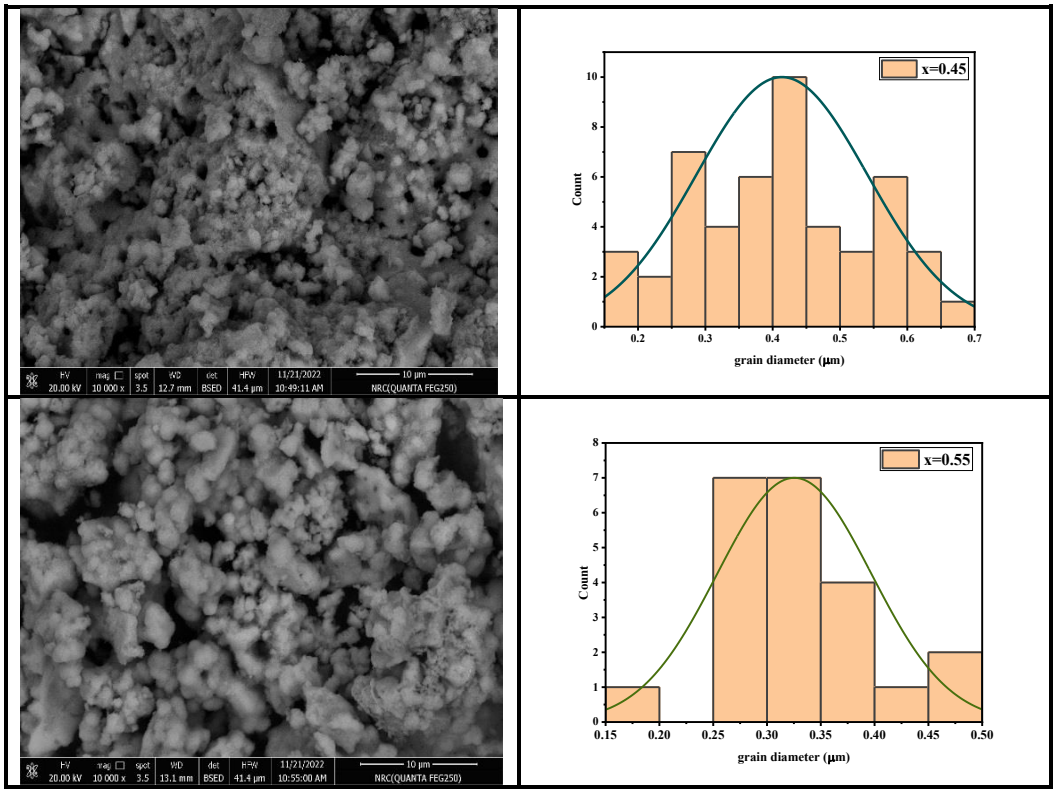

Fig. 4 SEM images and grain size histogram for $Ni_{0.3}Zn_{0.7-x}Mn_xFe_2O_4$ (x = 0, 0.15, 0.25, 0.35, 0.45, 0.55) ferrite samples.

Table (5). The grain size for $Ni_{0.3}Zn_{0.7-x}Mn_xFe_2O_4$ samples for different Mn content.

x	Grain Size (μm)
0	0.74
0.15	0.61
0.25	0.51
0.35	0.48
0.45	0.41
0.55	0.33

3.4 The dielectric properties as a function of frequency:

3.4.1 Dielectric constant (ε′ and ε″):

The frequency-dependent spectra of the real part (ε′) and the imaginary part (ε″) of the dielectric, for the Ni-Zn-Mn ferrite samples, are depicted in **Fig. 5** and **Fig. 6,** respectively. The measurements were conducted over the frequency range from 10^{-1} to 10^{7} Hz at room temperature. The dielectric parameters as a function of frequency can be described as ε′ and ε′′ which reflect the energy stored and the energy loss of the dielectric patterns, respectively.

At low frequency region, it is noticeable that ε` has high value and decrease sharply with the increase of frequency. A decrease in dielectric constant which may be due to the effect of interfacial polarization and space polarization suggested by Maxwell-Wagner role. The space charge polarization belongs to large charge carrier which is acted at low frequency and high relaxation time. At low frequency the dipole moment follows the external field leading to increase of the number of dipoles which contribute to the decrease of polarization.

At higher frequency the dipole doesn't follow the external field due to low relaxation time hence dielectric constant has low value constant near zero. At the region of high frequency, the space charge polarization is decreased at the hoping rate of charge carriers that drags the applied electric field which explain the reduction of ε′ value. Similar behavior was notices for ε′′ dielectric constant confirming that the real and imaginary part are independent on each other.

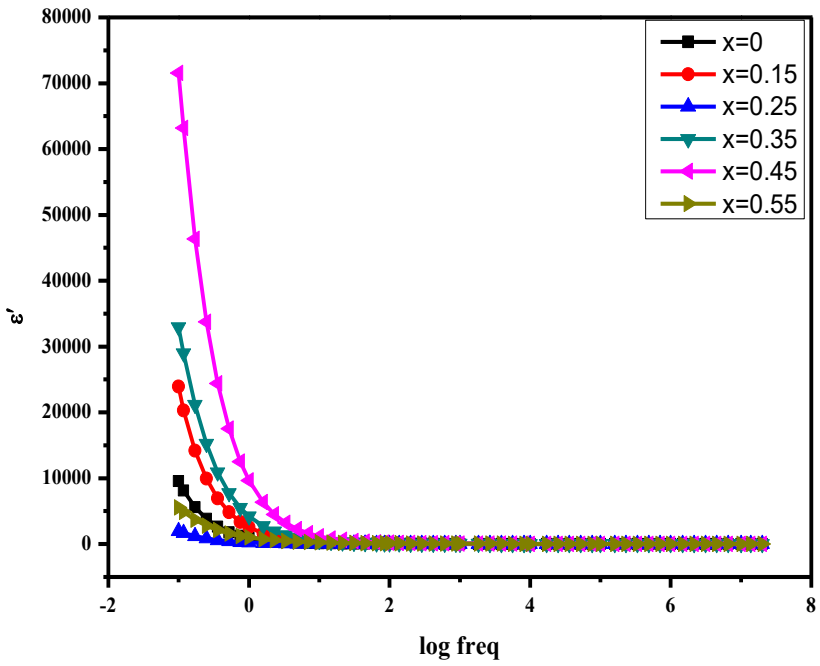

Fig. 5 The real part of dielectric constant of $Ni_{0.3}Zn_{0.7-x}Mn_xFe_2O_4$ for different Mn content.

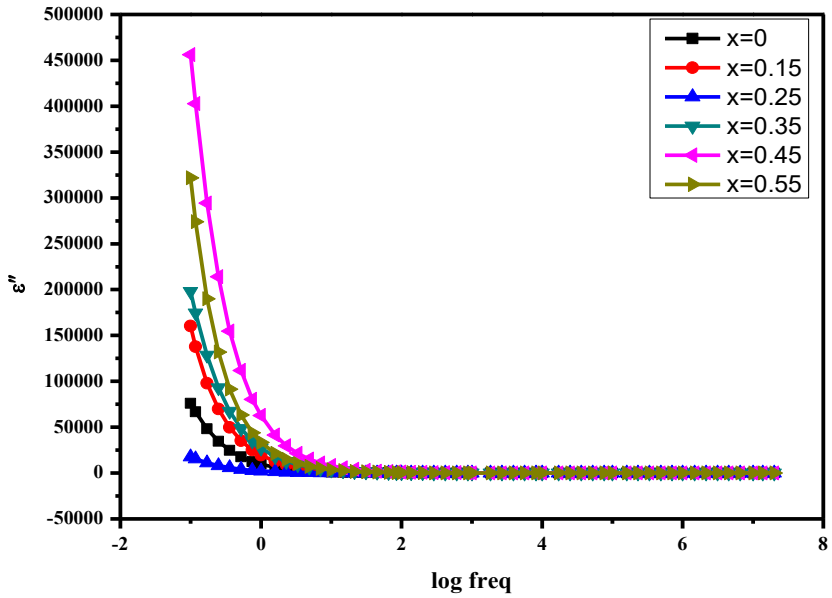

Fig. 6 The imaginary part of dielectric constant of $Ni_{0.3}Zn_{0.7-x}Mn_xFe_2O_4$ for different Mn content.

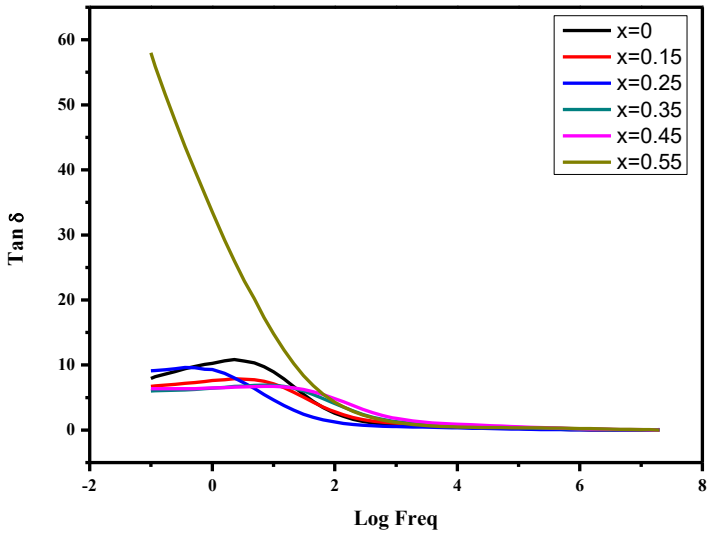

Fig 7 The dielectric loss as a function of frequency of $Ni_{0.3}Zn_{0.7-x}Mn_xFe_2O_4$ for different Mn content.

Table 6. The relaxation time for $Ni_{0.3}Zn_{0.7-x}Mn_xFe_2O_4$ for different Mn content at low frequency.

x (Mn content)	$T_m \times 10^{-2}$ (Sec)
0	6.5
0.15	3.9
0.25	26.4
0.35	1.4
0.45	1.1
0.55	166.7

The exchange sites for electron during hopping process between Fe^{3+} and Fe^{2+} **called the hopping process** . The hopping electron can follow the frequency of the external electric field leading to the appearance of a resonance peak at low frequency as shown . in Fig .7. The relaxation time were calculated and are given in table 6.

3.4.2 The electrical modulus (M′, M′′):

The frequency dependence of real M' and imaginary M′′ parts of dielectric modulus are shown in **Fig. 8** and **Fig. 9** at room temperature for Nano ferrite samples at different manganese content. In general, the M′ has an inverse behavior to ε′ and the polarization effect the dielectric modulus gives some information about the homogeneity of the polycrystalline sample and through light on the relaxation process in ferrite. The modulus curve has very small value near zero at low frequency due to the removal of the interfacial polarization which become negligible at low frequency. At high frequency region M` tends to increase with the increase of frequency.

The M" curve increases with applied frequency showing relaxation peak and end with sharp decrease at high frequency. The factors that affecting the behavior M′′ are the hoping mechanism, cation distribution, and grain size. The relaxation frequency and relaxation time can be deduced at maximum of M" curve.

The characteristic frequency responding to M′′ at maximum value is known as relaxation frequency. The value of relaxation time is giving by[22]:

$$\iota = \frac{1}{2\pi f_{peak}}$$

where F_{peak} is the frequency corresponds to the relaxation peaks. The calculated values of relaxation time are listed in Table (5) which ranged from 3.4×10-7 to 6.3×10-6 second.

The peak maximum is shifted to higher frequency and relaxation time to lower value with the increase of Mn concentration in Ni-Zn-Mn ferrite samples. This means that the position of this peaks depends on Mn content in the ferrite sample.

Table (7) The relaxation time values of $Ni_{0.3}Zn_{0.7-x}Mn_xFe_2O_4$ at high frequency

Sample	ι (second)
0	6.3×10^{-6}
0.15	5.3×10^{-6}
0.25	1.9×10^{-6}
0.35	2.2×10^{-6}
0.45	8.7×10^{-7}
0.55	3.4×10^{-7}

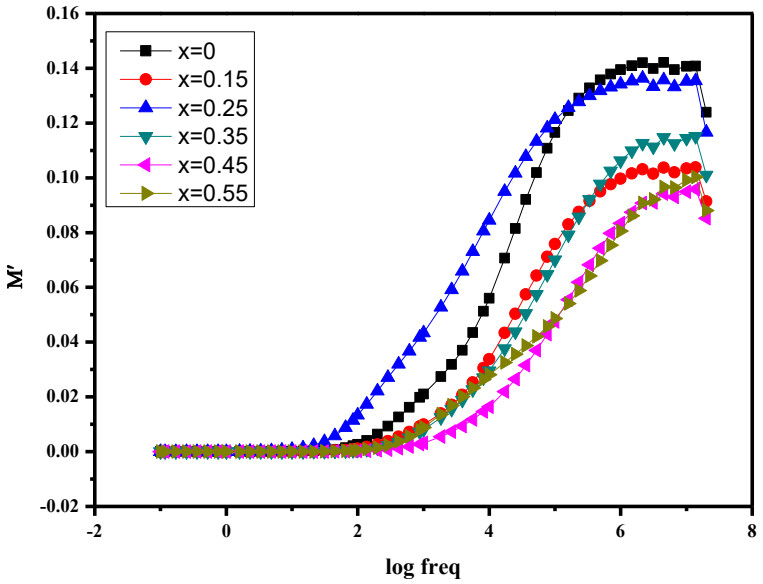

Fig. 8 The real part of the dielectric modulus of $Ni_{0.3}Zn_{0.7-x}Mn_xFe_2O_4$

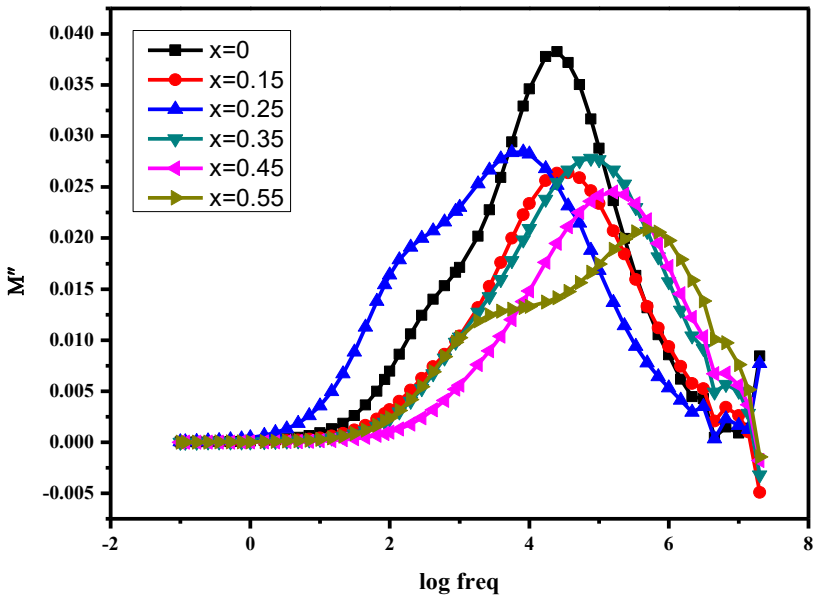

Fig. 9 The imaginary part of the dielectric modulus $Ni_{0.3}Zn_{0.7-x}Mn_xFe_2O_4$

The cole-cole diagram is obtained by plotting the imaginary part M'' vs real part M 'of electric modulus and is shown in **Fig. 10**. It illustrates the presence of semi-circles depending on the presence of the relaxation effect at low frequency. The effect of grain boundaries is more predominated whereas the predominate phenomenon at higher frequency is due to bulk resistance of the grains. It was noticed that the diameter of semi-circles decreases by the increasing of the Mn content as shown in **Table (8)**. The cole-cole diagram is Debye type if the semi-circles are formed whose center is lying on the real and non-Debye if the semi-circle is deviated from the horizontal axis. In our ferrite system the relaxation process is attributed to non-Debye type.

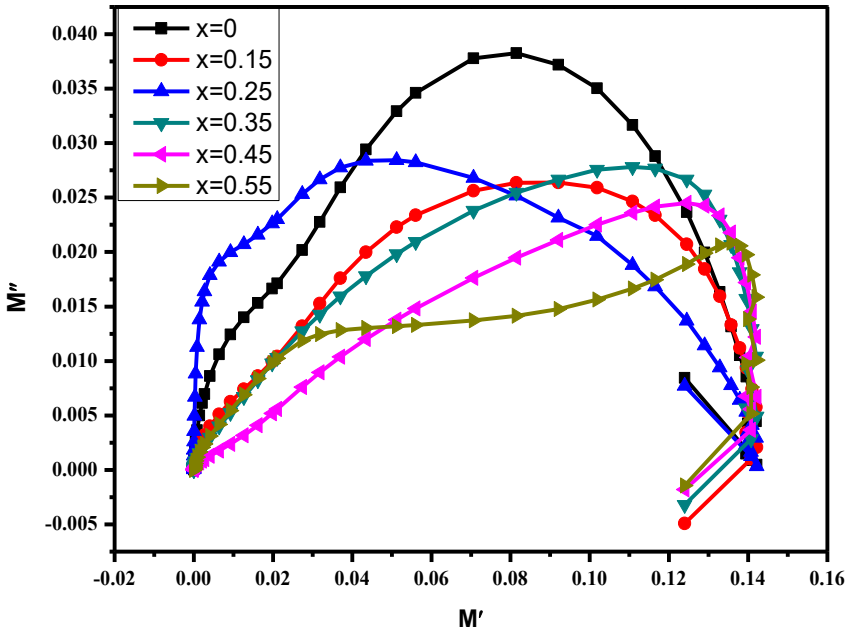

Fig. 10 The cole-cole diagram (M" vs. M') for $Ni_{0.3}Zn_{0.7-x}Mn_xFe_2O_4$

Table (8) Radius of semi- circle (cm) at maximum M" for $Ni_{0.3}Zn_{0.7-x}Mn_xFe_2O_4$.

x	Diameter (cm)
0	5.3
0.15	3.67
0.25	4
0.35	3.3
0.45	2.3
0.55	1.25

3.4.3 AC conductivity**:**

Fig. 11 and **Fig. 12** illustrate the variation of AC conductivity as a function of frequency for a series of $Ni_{0.3}Zn_{0.7-x}Mn_xFe_2O_4$ (x=0, 0.15, 0.25, 0.35, 0.45, 0.55) at room temperature. From

(σ′) figure it is noticeable that there are two regions. At low frequency region the conductivity is constant and almost equal zero representing σ′ is frequency independent (DC conductivity) up to10^3 Hz then it starts to increase gradually with the increase of frequency showing some dispersion. Also, the conductivity increases with the increase of Mn content. This behavior obeys to Jonscher's law [23]:

$$\sigma_{tot} = \sigma_{dc} + A\omega^n$$

where σ_{dc} is DC conductivity, which is frequency independent, A is temperature dependent factor with the electrical conductivity unites, ω angular frequency =2πf and n is the frequency exponent in the range of ($0 < n \leq 1$) and dimensionless. For n = 0 the electrical conduction is dc conduction, while n > 0, the electrical conduction is frequency dependent ac conduction. The low conductivity trend may be attributed to the grain boundaries with high resistivity which is more effective at low frequency causing law hoping rate of the charge carriers between Fe^{2+} and Fe^{3+} leading to the decrease of conductivity. While the grains of low resistivity become more effective at higher frequency hence the hoping rate of the charge carriers between Fe^{2+} and Fe^{3+} increases leading to the increase of the conductivity. σ" has the same behavior of σ` with frequency changes.

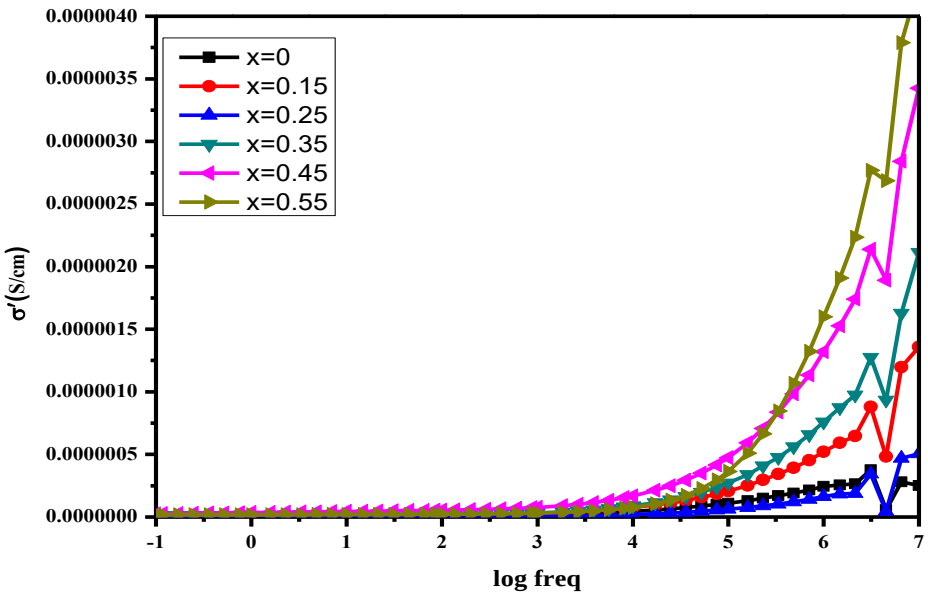

Fig. 11 The real part of ac conductivity as a function of frequency for different Mn content.

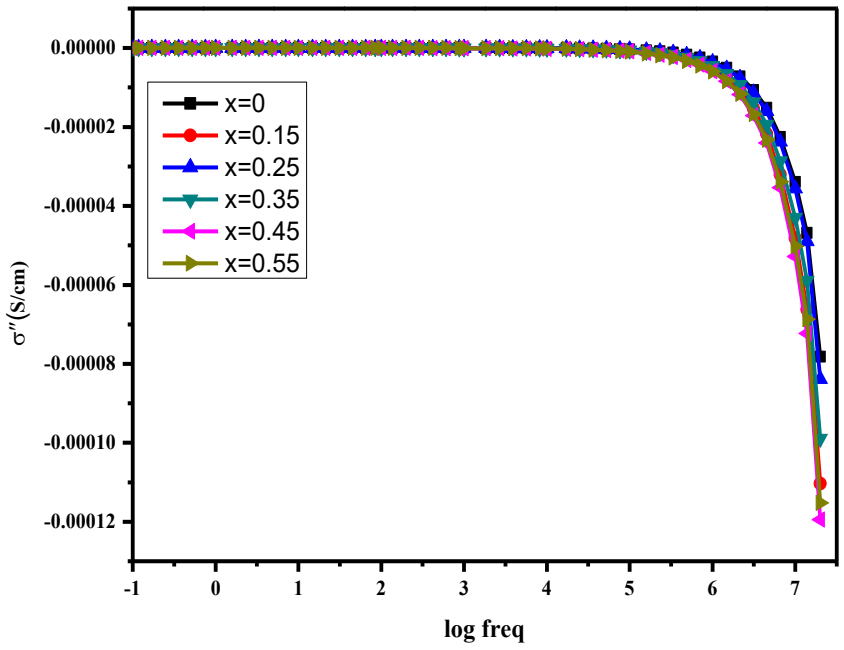

Fig. 12 The imaginary part of ac conductivity as a function of frequency for different Mn content.

3.4.5 The electric impedance:

The impedance spectroscopy is very important to analyze the relationship between the microstructure and the electrical properties and can study the effect of grains and grain boundary on the electrical properties of the material. **Fig. 13** represents the real part (Z´) and **Fig. 14** represents the imaginary part (Z´´) of the impedance Vs. frequency for the studied samples at different Mn content at room temperature.

It is noticeable that the electrical impedance has an inverse behavior to AC conductivity. At low frequency the impedance Z´ is very high then start to decrease with the increase of frequency to reach a constant value which is frequency independent. The value of Z' at different Mn^{2+} concentrations overlap at particularly high frequencies which refers to the probable liberation of space charges [24]. The impedance is high at low frequency as the grain boundary resistance is high which is dominate the grain resistance and overcome the grain resistance. At higher frequency the impedance is low because of the conductive behavior of grain.

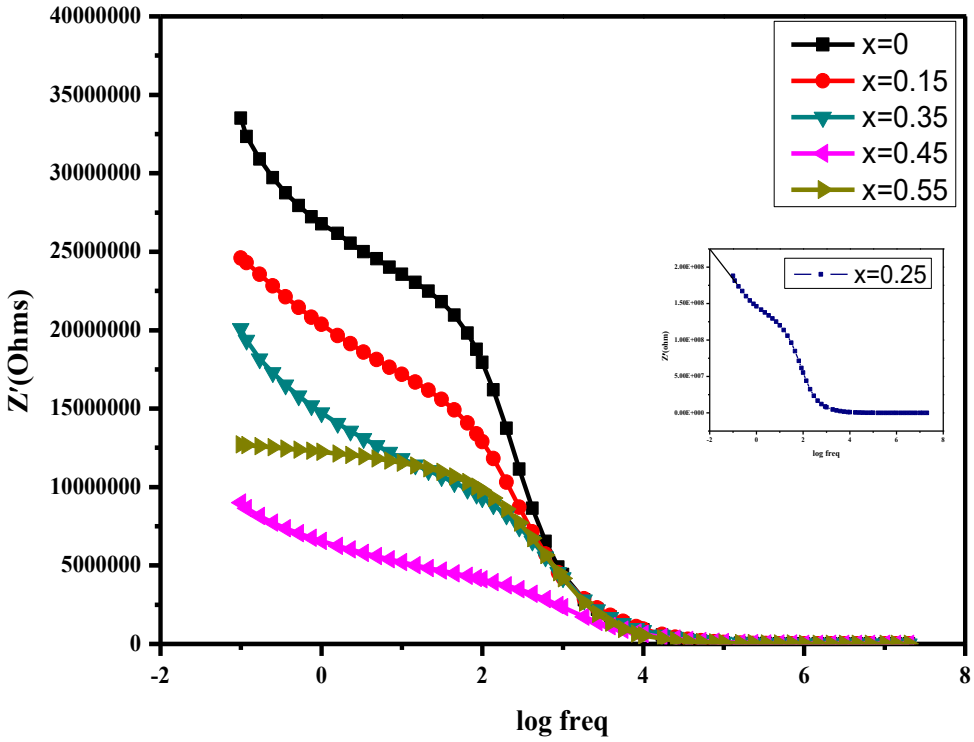

Fig. 13 The real part of electrical impedance for $Ni_{0.3}Zn_{0.7-x}Mn_xFe_2O_4$ for different Mn content.

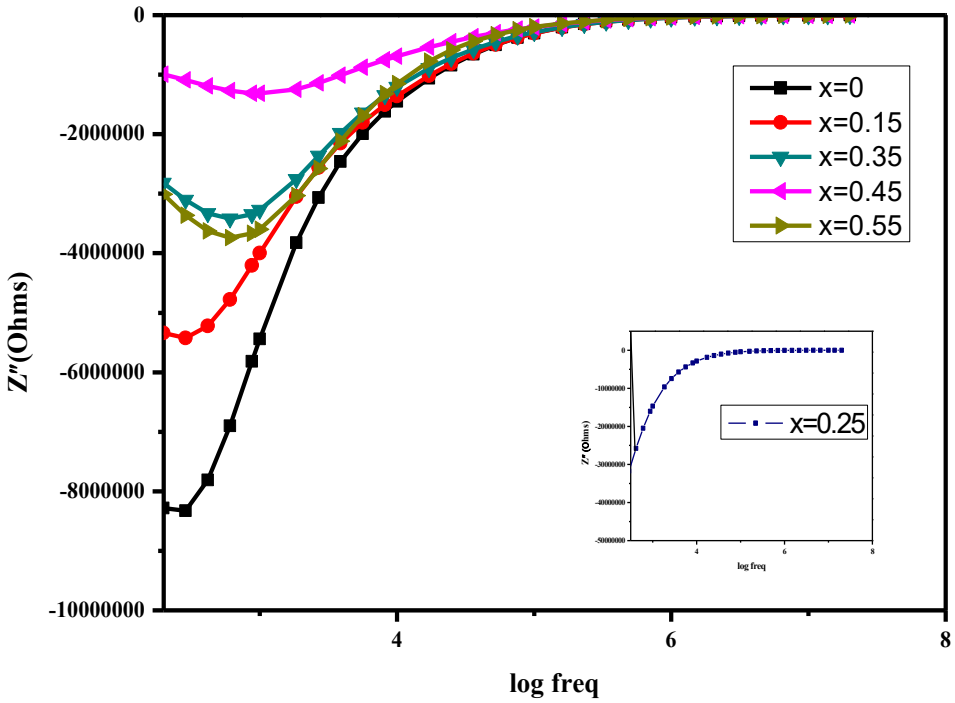

Fig. 14 The imaginary part of electrical impedance for $Ni_{0.3}Zn_{0.7-x}Mn_xFe_2O_4$ for different Mn content.

4. Conclusions

Nano-ferrite $Ni_{0.3}Zn_{0.7-x}$ $Mn_xFe_2O_4$ (x=0.00, 0.15, 0.25, 0.35, 0.45, and 0.55) were synthesized utilizing flash auto combustion method. The effect of Mn^{2+} substitution for Zn^{2+} in Ni-Zn ferrite was investigated. This paper is applying XRD, TGA, SEM analysis and dielectric properties as a function of frequency respectively. The Rietveld observed peaks correspond to two phases; spinel ferrites, belong to the Fd-3m space group, and hematite belongs to the R-3c space group. With increased manganese concentration, the spinel ferrites phase weight slowly decreases from 93.4% to 81.9% while the hematite phase weight is relatively low and increases varying from 6.6% to 18.1%. TGA shows two distinct regions, the first stage weight loss has the value range from 1 to 3 mg whereas for the second stage the weight loss ranges from 0.4 to 7 mg. The SEM micrographs reveal that the grain size is separated by pores which is clearly decrease by increasing Mn content, these phenomena is confirmed by x-ray analysis which state that the porosity decreased by increasing Mn content. The values of relaxation time ranges from 3.4×10^{-7} to 6.3×10^{-6} second. The electrical impedance has an inverse behavior to AC conductivity.

Data Availability Statement: The data that support the findings of this study are available on request from the corresponding author.

Conflicts of Interest: The authors declare no conflict of interest.

Declaration: All Authors declare that they have no funding sources for this research.

Compliance with ethical standards: This article does not contain any studies with human or animal subjects.

References:

[1] Nam P H et al., "Effect of zinc on structure, optical and magnetic properties and magnetic heating efficiency of $Mn_{1-x}Zn_xFe_2O_4$ nanoparticles," Phys. B *Condens. Matter* **550**, pp. 428–435, 2018,
doi: 10.1016/j.physb.2018.09.004.
[2] Arrasheed E A et al., "Dielectric, electrical, magnetic, and mechanical properties of Ni-Al ferrite/PANI composite films," Phase Transitions. **95**, pp. 803–822, 2022,
doi: 10.1080/01411594.2022.2117043.
[3] Kammar S S, "Rietveld Refinement and Study of Elastic Properties of Ni0.7Zn0.3DyxFe2-xO4 (0.0 ≤ x 0.03) Ferrite Nano-Structures," Int. J. Adv. Res. Sci. *Commun*. Technol **7**, pp 821–826, 2021,
doi: 10.48175/ijarsct-8320.
[4] Mostafa M et al., "Structure, Morphology and Electrical/Magnetic Properties of Ni-Mg ano-Ferrites from a New Perspective," Nanomaterials **12**, no. 7, 2022,
doi: 10.3390/nano12071045.
[5] Soufi A, Hajjaqui H, El. Moubarki R, Abdennouri M QOURZA S, and Barka N, "Spinel ferrites nanoparticles: Synthesis methods and application in heterogeneous Fenton oxidation of organic pollutants – A review," Appl. Surf. Sci. Adv **6**, pp. 100145, 2021,
doi: 10.1016/j.apsadv.2021.100145.
[6] Abdullah Dar, M, Shah, J, Siddiqui, W A, Kotnala, R K: Appl. Nanosci. **4**, pp. 675–682, 2014.
[7] Ko¨seog˘lu, Y, Bay M, Tan M, Baykal A, So¨zeri H, Topkaya R, Akdogan N J. Nanoparticle Res**13**, pp. 2235–2244, 2011.
[8] Yang H, Zhang X, Ao W, Qiu G, Mater. Res. Bull. **39**, pp.833–837, 2004.
[9] Jing J, Liangchao L, Feng X, J. Rare Earths **25**, pp. 79–83, 2007.
[10] Hussain A, Abbas T, Niazi S B, Ceram. Int. **39,** pp. 1221–1225, 2013.
[11] Hemeda O M, , Tawfik A, Mostafa M, Zaki M, Abd EL Ati M I, IOP Conf Series J. Phys. Conf. Series **1253**, pp. 012026, 2019.
[12] Stefanescu M, Stoia M, Stefanescu O, Dippong T, Barvinschi P, Acta Chim. Slov. **56,** pp. 379–385, 2009.
[13] Dippong T, Cadar O, Levei E A, Deac I G , Goga F, Borodi G, Barbu-Tudoran, L.: Ceram. Int. **45**, pp. 7458–7467, 2019,
[14] D'souza A, Deepak Kumar M, Chatom M, Naik V, Naik P P, Tangsali, R. B.: Adv. Sci. Lett. **22**, pp. 773-779, 2016.

[15] Mohanty P, Prinsloo C J, Sheppard, and W. D. Roos, “Effect of Fe substitution on structural and A. R. E magnetic properties of NiCr2O4,” *Acta Phys. Pol. A*, **133**, pp. 574–577, 2018,
doi: 10.12693/APhysPolA.133.574.
[16] Eltabey M M, Agami W R, and Mohsen H T, “Improvement of the magnetic properties for Mn-Ni-Zn ferrites by rare earth Nd3+ ion substitution,” *J. Adv. Res.*, 5, no. **5**, pp. 601–605, 2014,
doi: 10.1016/j.jare.2013.08.005.
[17] Mane D R, Birajdar S E, Shirsath R A, Telugu, and Kadam R H, “Structural and magnetic characterizations D. D of Mn-Ni-Zn ferrite nanoparticles,” *Phys. Status Solidi Appl. Mater. Sci* **207**, pp. 2355–2363, 2010.
doi: 10.1002/pssa.201026079.
[18] Abdel M I A, Maksoud G S, El-Sayyad A, Abokhadra L I,. Soliman, H. H. El-Bahnasawy, and A. H. Ashour, “Influence of Mg^{2+} substitution on structural, optical, magnetic, and antimicrobial properties of Mn–Zn ferrite nanoparticles,” *J. Mater. Sci. Mater. Electron.*, **31**, no. 3, pp. 2598–2616, 2020,
doi: 10.1007/s10854-019-02799-4.
[19] Flaifel M H et al., Preparation, thermal, magnetic and microwave absorption properties of thermoplastic natural rubber matrix impregnated with NiZn ferritenanoparticles,” *Compos. Sci. Technol.* **96**, pp. 103–108, 2014,
doi: 10.1016/j.compscitech.2014.03.016.
[20] Nasr M H, Elkholy M M, El-Deen L M S, Abouhaswa A S, Turky G M, and EL-Hamalawy A A, “A comprehensive study on crystal structure, magnetic, and electrical properties of Ni-doped Fe–Cd spinel nano-ferrites,” *J. Mater. Sci. Mater. Electron* **33**., pp. 15652–15664, 2022,
doi: 10.1007/s10854-022-08469-2.
[21] Hemeda O M, Mostafa N. Y., O. H. Abd Elkader, D. M. Hemeda, A. Tawfik, and M. Mostafa, “Electrical and morphological properties of magnetocaloric nano ZnNi ferrite,” *J. Magn. Magn. Mater.*, vol. 394, pp. 96–104, 2015, doi: 10.1016/j.jmmm.2015.05.059.
[22] Dielectrics T O N, Alma Mater Studiorum Università di Bologna D . Cornigli et al., Characterization of dielectric properties and conductivity in encapsulation materials with high insulating filler contents”,” no. May, 2024.
[23] Anupama M K, Rudraswamy B and Dhananjaya N, Investigation on impedance\response and dielectric relaxation of Ni-Zn ferrites prepared by self-combustion technique, *J. Alloys Compd*. **706**, pp. 554–561, 2017,
doi: 10.1016/j.jallcom.2017.02.241.
[24] N. S. Al-Bassami and S. F. Mansour, “AC conductivity, complex impedance and photocatalytic applications of Co2+ substituted Mg–Zn nanoferrite,” *Appl. Phys. A Mater. Sci. Process.*, vol. 127, no. 1, pp. 1–13, 2021,
doi: 10.1007/s00339-020-04022-2.